Finite element analysis study on the thermomechanical stability of thermal compression bonding (TCB) joints in tubular sodium sulfur cells

Keeyoung Jung [a], Solki Lee [b], Yoon-Cheol Park [a], Chang-Soo Kim [b],*

[a] Energy Storage Materials Research Center, Research Institute of Industrial Science and Technology (RIST), Pohang, Kyungbuk 790-060, South Korea
[b] Materials Science and Engineering Department, University of Wisconsin–Milwaukee, Milwaukee, WI 53211, USA

HIGHLIGHTS

- We introduce FEA model to predict the thermal stress concentration of NaS batteries.
- Shear stress accumulation can be critical to the joint failure of NaS batteries.
- Types and geometries of joint/container materials can reduce the thermal stress.

ARTICLE INFO

ABSTRACT

A typical large capacity sodium sulfur (NaS) battery is operated at 300–350 °C with 20–50 °C thermal fluctuations during its charging and discharging. In addition, for maintenance purposes, the cell experiences larger temperature changes down to the intermediate or room temperatures. Such temperature changes can cause mechanical failure of heterogeneous joints such as thermal compression bonding (TCB) joints, which is one of the most critical issues in developing NaS batteries. The present study seeks to build a computational finite element analysis (FEA) model to predict the thermomechanical responses of NaS batteries to the attack induced by the temperature changes. Specifically, the thermomechanical stress accumulation at TCB joints of a tubular cell has been explored during its booting-and-shutdown cycles. Static temperature profiles and simplified friction conditions in the cathode wall were assumed for the model. Using the developed model, the stress components that dominantly contribute the stress accumulation at the joint were identified, and the effects of TCB geometries and container material types on the thermal stress accumulation at the TCB joints were carefully examined. It turns out that the stress accumulation at the bonding interface would be critical for the failure at the TCB joints.

© 2013 Elsevier B.V. All rights reserved.

1. Introduction

Since Weber and Kummer first introduced a sodium sulfur (NaS) cell for electric vehicle (EV) applications in 1967 [1], the battery has drawn a great attention because of its advantages such as low cost, long discharge time (up to eight hours at its full power), capability to have high energy capacity (up to larger than 1200 Wh per cell), long lifetime (over 15 years), and high specific and volumetric energy densities (222 Wh kg^{-1} and 367 Wh L^{-1}) [2–4]. In addition, this highly efficient battery is recognized as very attractive for commercialization because they are manufactured using relatively cheap materials, such as sodium (Na), sulfur (S), aluminum (Al) alloys, steels, carbon (C), alumina (Al$_2$O$_3$), and so on [5].

In the early years between the late 60's and early 90's, various sized battery designs were proposed as promising candidates for EV and space applications. However, none of these designs has been commercially successful mainly due to the safety issues. This safety issue in NaS batteries stems from the facts that, (*i*) the anode and cathode active species, i.e., Na, S, and sodium polysulfides (Na$_2$S$_x$, where *x* ranges from 3 to 5) are in a molten state at cell operation temperatures of 300–350 °C, (*ii*) the solid electrolyte of β/β″-Al$_2$O$_3$, that also functions as a separator, is a thin and fragile ceramic material, and (*iii*) the bonding area between the heterogeneous components, such as thermal compression bonding (TCB) joints between metal and ceramic components, and glass sealing (GS) joints between α- and β-alumina ceramics, could be weak due

* Corresponding author. Materials Science and Engineering Department, University of Wisconsin–Milwaukee, 3200 N. Cramer St., Milwaukee, WI 53211, USA. Tel.: +1 414 229 3085; fax: +1 414 229 6958.
E-mail address: kimcs@uwm.edu (C.-S. Kim).

to the high thermal strains driven by freeze/thaw cycles. The safety issue, therefore, can arise when the ceramic electrolyte or the heterogeneous joints are broken, which will lead to direct electrochemical reactions between active materials or oxidation of active materials resulting in a large amount of heat release. A thermodynamic calculation (using HSC chemistry, version 7.1, Outotec, Inc.) indicates that enormous enthalpy changes up to 7.6 MJ in the case of a large cell will occur by forming Na_2S_x, Na_2O, and etc. For example, when Na_2S_4 (l) and Na_2O (s) are formed from the direct reaction between Na (l) and S (l) at 350 °C, and from oxidation of Na (l) via O_2 (g), the enthalpy changes are −356.7 and −359.7 kJ mol^{-1}, respectively. The operation temperature of NaS is generally maintained at 300−350 °C, (*i*) to avoid the solidification of Na_2S_x that are electrochemical reaction products during discharging [6], and (*ii*) to effectively transport cations (Na$^+$) through the solid electrolyte (β/β″-alumina) that shows low ionic conductivities at lower temperatures. Although a number of prior efforts have been made to lower the operation temperature to improve their stability and secure the safety [7–9], these technologies still need to be further improved for commercial applications.

Fig. 1(a) illustrates a cross-sectional view of a typical tubular NaS cell, and Fig. 1(b) shows the enlarged image of its header and bottom areas along with indicating cell components. Fig. 1(c) is the cropped area amplified from the dotted square in Fig. 1(b). As shown in Fig. 1(b) and (c), the header area of a tubular NaS cell is composed of various structural components such as an insulating ring (α-alumina), solid electrolyte (β/β″-alumina), sodium cartridge, cartridge cover, cartridge cap, collar, bracket, cell container, and etc. The insulating ring is used to electrically separate the electrodes, the GS joint is to bond between α- and β-alumina, and the TCB joints are bonding between the insulating ring and metallic parts, respectively.

During its lifetime of 15−20 years, a cell can be subjected to multiple booting-and-shutdown cycles; upon booting, the cell temperature is increased from 20 °C (i.e., ambient temperature) to 300−350 °C (i.e., operation temperature), and the cell needs to be cooled down to intermediate or room temperatures for maintenance purposes. The temperature difference ($\Delta T = 280–330$ °C) can lead significant thermomechanical stress, in particular to the header area because they consist of various materials that feature different coefficients of thermal expansion (CTE) from one another. Consequently, the components in the header can suffer from high stress accumulation in conjunction with severe elastic/plastic deformation that can cause failure in parts or joints. Such thermomechanical stress accumulation becomes more serious as the cell size becomes larger because the applied thermal strain would be qualitatively proportional to the cell dimension. Therefore, in the
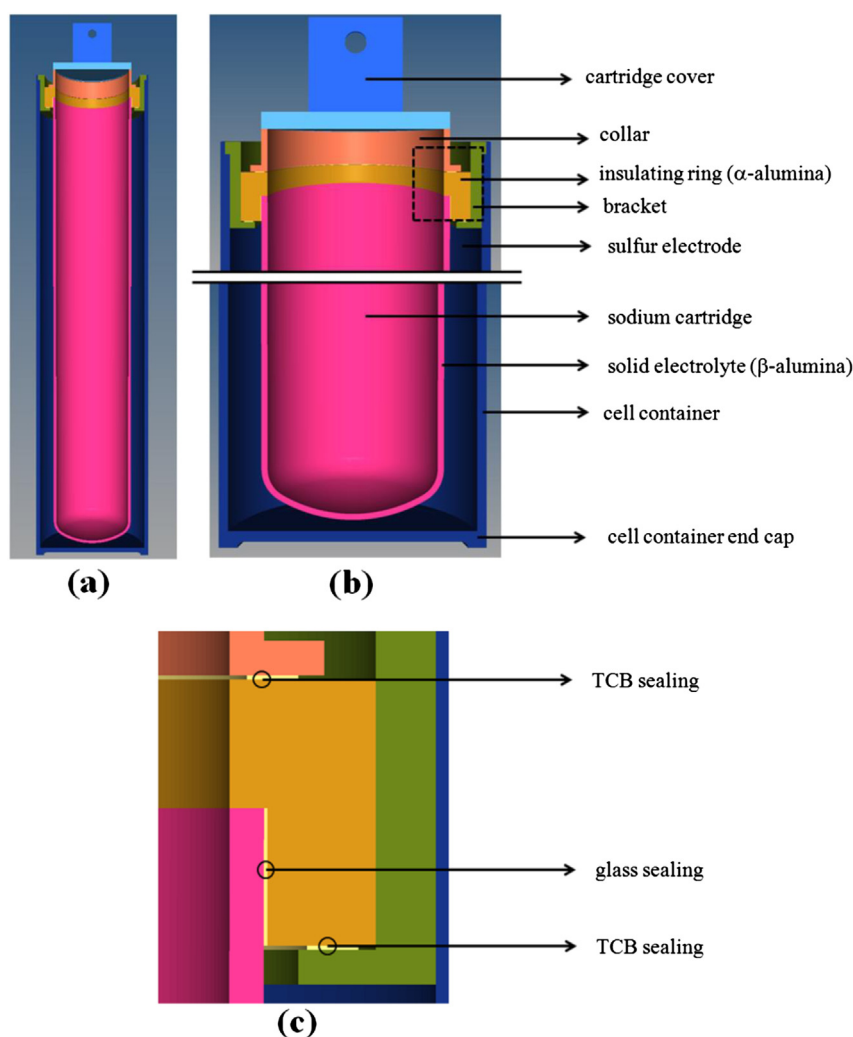

Fig. 1. Schematic cross-sectional structure of a typical tubular NaS battery to show (a) the entire cell, (b) enlarged cell header and bottom regions, and (c) cropped section for TCB insert metal and GS joints. The dotted square box in (b) corresponds to the cropped image of (c).

medium-to-large size cells (i.e., 300–600 mm in height) for grid scale energy storage applications, it is essential to understand the thermomechanical behavior and its consequences on the failure. In fact, such a fracture issue at the joints is regarded as one of the most important factors in designing medium-to-large size NaS cells. Typical failure modes at the TCB joints fall in the following two categories, depending on the bonding strength between the insert metal and the ceramic part, and the fracture toughness and surface defect sizes of the insulator ceramic parts: (i) interfacial failure at the insert metal/ceramic interface, and (ii) bulk failure through the ceramic part, respectively. The in-house measurement data from the first five discharging/charging cycles of a NaS cell used in this study are presented in Fig. 2 to show the (a) voltage changes versus the depth of discharge (DoD) and the (b) temperature profiles during the heating (booting) and cooling (shuttingdown) processes. It is seen that the temperature of the cell ranges from 20 to about 350 °C.

Bearing in mind that the stress aggregation at the joints is important, we introduce a computational tool to predict and understand the thermomechanical responses in the header area of medium-large size tubular NaS cells. An *in silico* computational approach is essential in understanding the stress accumulations in the cells as *in vivo* experimental measurements are practically difficult, labor-intensive, time-consuming, and very expensive. Adopting an analytical estimation approach is also non-trivial because the NaS cell is composed of a number of parts, and because material properties of metallic parts, including moduli and stress–strain relationships, contain a wide range of variations with temperatures that cannot be easily incorporated into the analytical model. Therefore, development of a reliable and robust computational prediction model may allow us to diagnose the current situations and it will guide the advanced materials/geometrical designs of NaS cells. In this paper, a finite element analysis (FEA) computational approach has been applied to a representative prototype tubular NaS cell to address the stress concentration issues in the header area. In particular, because failures at or near TCB joints are frequently observed, thermomechanical stress distributions during the booting-and-shutdown thermal cycles at the TCB joints and their integration to the surrounding ceramic materials are carefully examined.

2. Finite-element analysis (FEA) computations

2.1. Mesh generation

A commercial ABAQUS FEA software package (version 6.11, Simulia Inc.) has been employed to develop a model for the thermal stress prediction. The cell design used in the present study is shown in Fig. 3. To create a representative tubular NaS cell for FEA, the digitized image was generated using the Rhinoceros (version 5.0, McNeel Inc.) auto computer-aided design (CAD) software, as shown in Fig. 3(a). In this model, the outer radius and height of a cell were set as 43 and 375 mm, respectively. It needs to be noted that the design shown in Fig. 3(a) is a simplified version that contains only typical features of a conventional NaS cell, and other components such as the wick tube, the carbon felt, etc., that may not directly influence the stress concentration in the header are omitted. The cross-sectional images given in Fig. 1 also are based on this simplified cell design. The dimensions of some components are substantially smaller than that of the cell size; for example, the
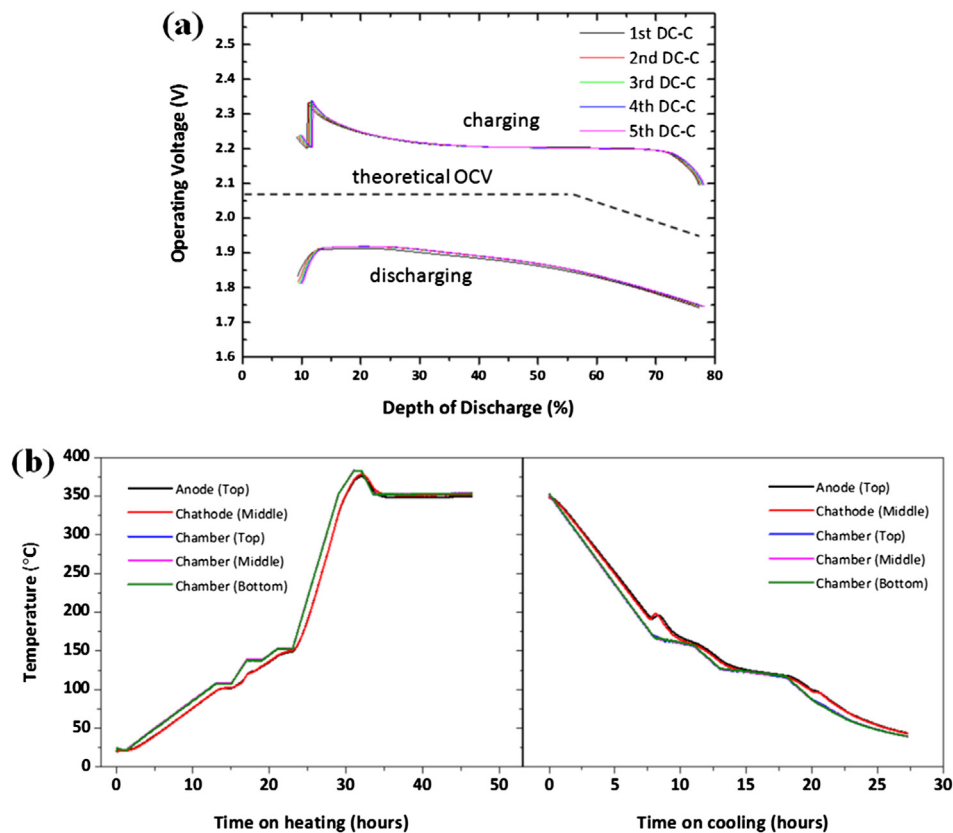

Fig. 2. NaS cell characteristics used in this study, (a) a voltage versus the depth of discharge (DoD) curves during the early stage charge/discharge cycles (5 cycles) when the cell has been discharged down to 78% DoD, (b) temperature changes as a function of heating/cooling times in various locations inside the cell. the theoretical open circuit voltage (OCV) is also provided in (a).
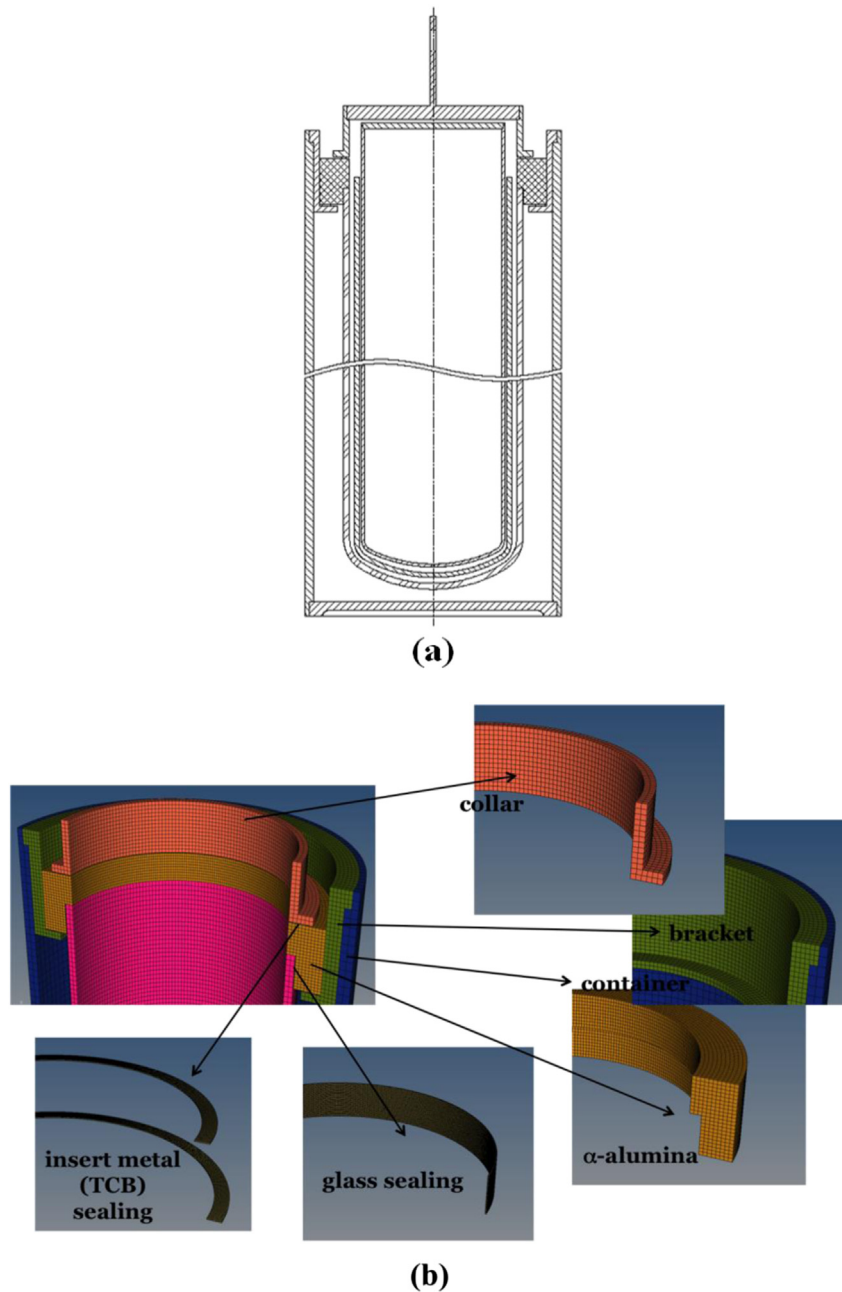
Fig. 3. FEA mesh generation procedure to show (a) digitized image of the representative prototype NaS battery design, and (b) examples of FEA mesh elements for selected parts in the header area of a tubular NaS battery.

thickness of a β-alumina electrolyte tube (2 mm) is much smaller than the height of the tube (342 mm), and the thicknesses of TCB insert metals (0.25 or 0.5 mm) and/or glass sealing (0.2 mm) are considerably smaller than the height of cell (375 mm). Such a multi-scale FEA mesh scheme incorporating the size differences among the components must be adequately accommodated into the computational model development to relevantly predict the thermo-mechanical responses to the temperature changes. As illustrated in Fig. 3(b), the FEA elements for each component were created using commercial mesh generation software (hyperMesh, version 10.0, Altair Engineering, Inc.). In this figure, amplified images of FEA meshes for an α-alumina insulating ring, β-alumina tube and other components forming TCB and GS joints, are also shown in the same scale, which identifies the FEA mesh size

differences between the cell components. An optimized mesh size was selected to produce consistent results with a minimum number of elements. In the present model, the hexahedron-type mesh was used for all parts, and the total number of FEA elements for the entire battery system was 442,918. A full three-dimensional FEA method was adopted; it is anticipated that this full three-dimensional model can be readily applied in the future work to incorporate any potential anisotropic features along the circumferential direction of the cell.

2.2. Material properties

A tubular NaS cell is made of a number of different materials, including aluminum (Al) alloys, stainless steels (STS), α- and β/

β″-alumina (Al₂O₃), glass, carbon, iron—chromium (Fe—Cr) alloys, and more. It is important that as accurate as possible thermo-mechanical properties of these different types of materials at the temperature range of 20—350 °C needs to be incorporated into the computation. Fig. 4 shows the changes of the CTE, elastic modulus, and true plastic stress—strain with increasing temperatures of an Al alloy (Al3003), stainless steel (STS430), α-alumina, β/β″-alumina, and a glass sealant used in this work [10]. Al alloys and steels are commonly used in NaS cells for structural parts (i.e., container, TCB insert metal, bracket, collar, and more) because of their low price, good machinability, and good weldability. From Fig. 4(a) and (b), it is apparent that the metallic (Al3003 and STS430) and ceramic (α- and β/β″-alumina) parts exhibit signifi-cantly different CTEs and elastic modulus from one another. Also, a considerable difference in true plastic deformation behaviors in Al3003 and STS430 materials shown in Fig. 4(c) and (d) indicates that the resultant thermomechanical stress distribution would be greatly influenced by the selection of constituent materials. In the present study, Al3003 was selected as a standard structural ma-terial, and the effects of container alloys (i.e., Al3003 vs. STS430) with different CTEs on stress accumulations at the TCB joints have been also examined. Table 1 summarizes the thermomechanical properties of materials incorporated in the current computational model. These properties were measured or obtained through the existing literature [10].

2.3. Computation conditions

A thermally static computation condition was assumed for the FEA throughout this work; it was hypothesized that the effects of

Table 1
Summary of physical and thermo-mechanical properties of materials in the header area of typical tubular NaS battery systems.

	Modulus of elasticity (GPa)	Poisson's ratio	CTE ($\times 10^{-6}$/K)	Stress—strain data
Al3003	Temperature dependent (refer to Fig. 4)	0.33	Temperature dependent (refer to Fig. 4)	Temperature dependent (refer to Fig. 4)
STS430		0.28		
α-Alumina		0.23		Elastic
β-Alumina		0.23		
Glass	62	0.22	6.9	

the transient electrochemical reactions involving endothermic or exothermic reactions during its service can be ignored, and that a NaS cell immediately reaches its static thermal equilibrium without internal temperature gradients at the temperature of interest. This assumption is not unrealistic considering that the heating and cooling processes for booting and shutdown, respectively, are very slowly controlled (30—50 h, see Fig. 2(b)) to prevent any thermal shock that could potentially yield mechanical failure and/or disin-tegration of components. In addition, since the header assembly experiences high temperatures up to 550 °C for a relatively long time during TCB process, the residual stress in the metallic TCB joints could be assumed to be small, and accordingly the influences of residual stresses in the sealing metals were not taken into consideration in the computation. Additionally, as stated before, the effect of the carbon/glass felt placed in the cathode compart-ment was also ignored.

Fig. 5(a) illustrates the temperature profile applied to the computation. We have tested two thermal cycles of booting-and-shuttingdown processes to study the effect of the cycle numbers
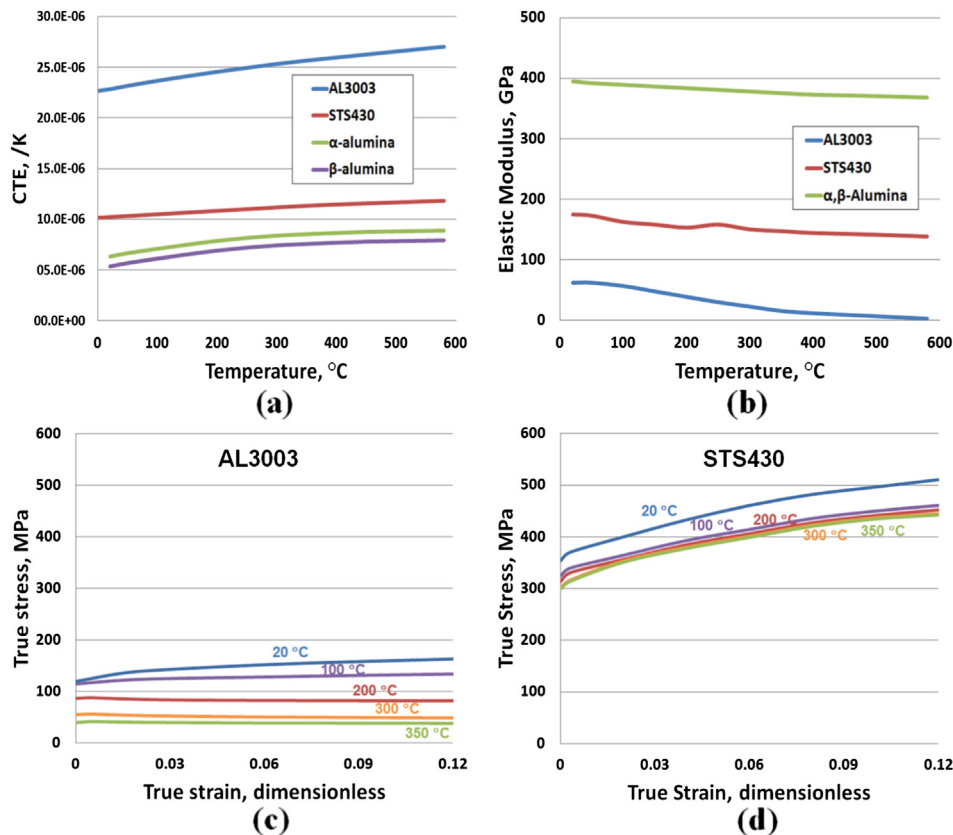

Fig. 4. Material properties used in the computation to show (a) CTE values, (b) elastic modulus values, (c) true plastic stress—strain curves for Al3003, and (d) true plastic stress—strain curves for STS430 at the temperature range of 20—350 °C, respectively.
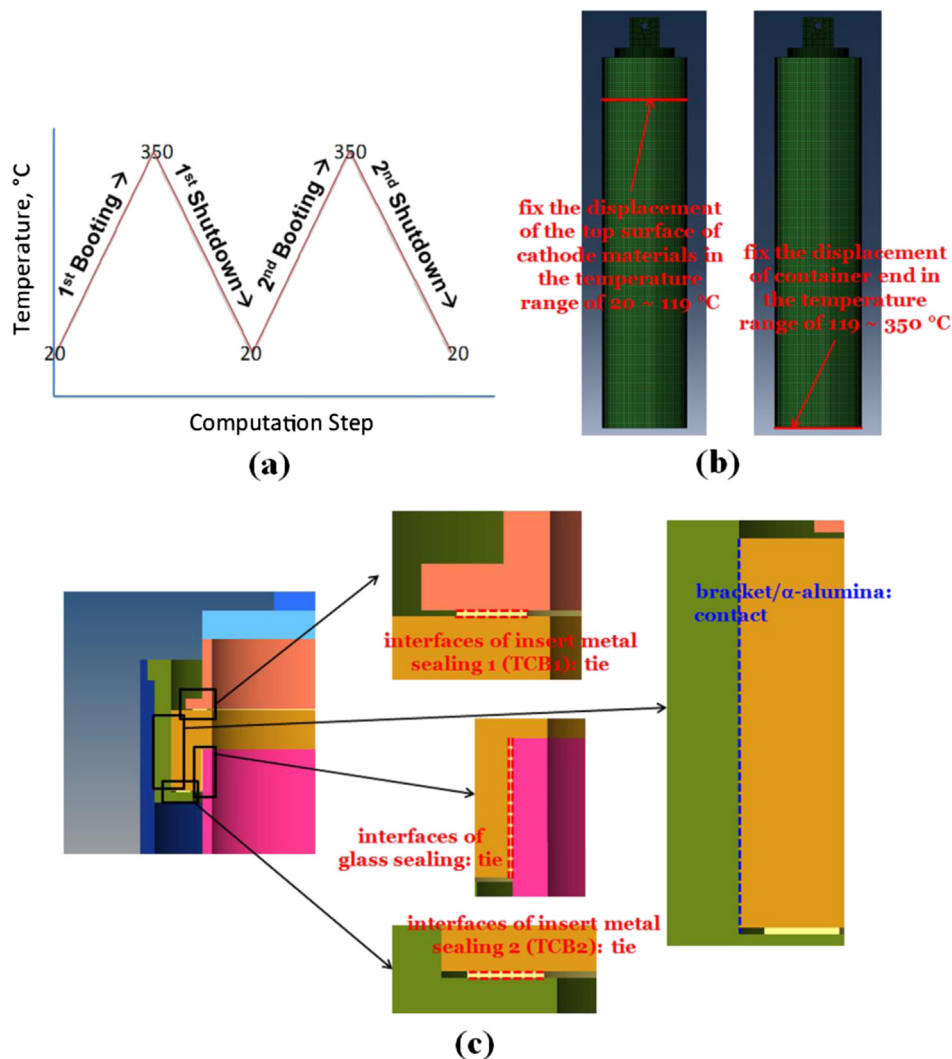
Fig. 5. Computation conditions to show the (a) temperature profile indicating the initial, operation, and maintenance/cleaning temperatures, (b) boundary conditions (BC) upon heating and cooling of the NaS system, and (c) interface conditions (i.e., "tie" and "contact" conditions) in the battery header area.

on the stress distributions and concentrations in the vicinity of the TCB area. It is important to understand the quantitative relationships between the number of shutdowns for maintenance and the resultant stress distributions in the cell, because more plastic stress will be accumulated with the number of shutdowns and multiple booting-and-shuttingdown processes are expected during the service life. The operation and maintenance temperatures are set as 350 and 20 °C, respectively. As for the boundary condition (BC) to reflect geometrical constraints, we have fixed the displacement of the top surface of cathode materials and the displacement of the container end in the temperature ranges of 20–119 and 119–350 °C, respectively. Such BCs are graphically shown as red (in web version) solid lines in Fig. 5(b). These are intended to incorporate the phase transformation effect of cathode materials (sulfur) at 119 °C. For example, upon cooling, if the system temperature reaches 286 °C, polysulfides (Na_2S_x) start to be solidified, and if the temperature continues to decrease to 119 °C, then liquid sulfur (if there is any) will also be solidified. In the present work, it is assumed that the cathode material in the solid state imposes a very strong friction on the interface between the sulfur and container to essentially lock the displacement along the circumferential line of the top surface of the sulfur and electrolyte. The volume changes of the container, thus, are included in the model under different situations (i.e., liquid and solid

states) of cathode materials. Such assumption is reflected to the fixed BC in the range of 20–119 °C. To confirm the validity of the BC, it was also carried out a series of FEA computations with free expansion conditions; it was found that the differences in the results of these two different BCs fall within about an 8% error range. Thus, the maximum computation error attributed to these assumptions is estimated as 8%. It is considered that the slumping (i.e., formation of solid polysulfides and their accumulation at the bottom of the cathode compartment) may contribute the thermal stress distributions. More advanced model development including the slumping effect is currently in progress. All other outer surfaces of the cell remained in the free BCs throughout the computation. Fig. 5(c) describes the interface conditions applied to the header area. Assigning adequate interface conditions is also important to predict reliable stress distributions. As designated in red dotted lines in Fig. 5(c), the interfaces of TCB insert metal and glass sealing joints are treated as non-sliding (i.e., "tie" condition) mode. Along other surfaces in the header area, such as the interface between the bracket and insulating ring, a sliding (i.e., "contact" condition) mode was imposed as indicated in blue dotted lines in the figure. For convenience, the TCB joints positioned above and below the insulating ring are named TCB 1 and TCB 2, respectively. Free expansion conditions were assigned along the outer boundaries of the container except temperature

dependent BCs described in Fig. 5(b). For efficient convergence of calculations, a static implicit iteration method was used with an increment of 0.025 of each computation step.

3. Results and discussion

3.1. Stress distributions in TCB joints

In Fig. 6, we show an example of contours for the von-Mises stress distributions (a) before the 1st booting (20 °C, initial condition), (b) after the 1st booting (350 °C, operation condition), (c) after the 1st shutdown (20 °C, maintenance condition), (d) after the 2nd booting (350 °C), and (e) after the 2nd shutdown (20 °C). In the figure, von-Mises stress distributions are shown using the color legend with minimum and maximum values of 0.0 and 5.328×10^2 MPa. As addressed in the "Materials properties" section, an Al alloy (Al3003) was selected as a container material in this case. Fig. 6 shows that as the temperature increases to the operation temperature, the von-Mises stress increases in the header area along the inner circumference of β-alumina tube (sky blue (in web version) contrast in Fig. 6(b)), and as temperature decreases to the maintenance temperature, the concentration of maximum von-Mises stress is observed along the circumference of the top surface of a cathode region (red color in Fig. 6(c)). It is resulted from the high friction and strong adhesion between the solid sulfur and electrolyte/container near the top surface of the active cathode materials in the lower temperature regime. A similar trend in the stress distribution is predicted as the heating-and-cooling cycle is repeated in Fig. 6(d) (after the 2nd booting, 350 °C) and Fig. 6(e) (after the 2nd shutdown, 20 °C). Therefore, it can be postulated that a NaS cell using Al3003 as a container material will experience the highest stress concentration at room temperature after service.

To analyze the thermomechanical response at the TCB joints, we have used the conventional polar coordinate notation as defined in Fig. 7(a) for the stress and strain tensors in the cylindrical coordinate system. The radial direction from the axis symmetry line to the outer container, the cell circumferential direction, and the cell height (vertical length) direction were assigned as 1, 2, and 3 for the two-digit tensor notations, respectively. Therefore, 11, 22, 33, 12, 13, and 23 tensors denote the radial normal, circumferential normal, height normal, circumferential shear, radial shear, and height shear components of the stress and strain tensors, respectively. When Al3003 was used as a container material, the distributions of the average normal and shear stress components on the top surface of TCB 2, as the cell temperature changes, are plotted in Fig. 7(b) with reference to the radial, circumferential, and height directions of the cell. The stress profiles shown in Fig. 7(b) were obtained by averaging all of the stress data on the top surface FEA mesh of TCB 2. The stress component data for TCB 2 have been presented first because the stress aggregations in TCB 2 for the cathode sealing are, in general, higher than those in TCB 1 for the anode sealing, which will be further discussed in the next paragraph. In addition, it should be mentioned that the TCB plane facing against the ceramic insulator ring experiences more stress concentrations compared with other faces that are adjacent to the metallic parts (i.e., collar or bracket), as there are relatively larger CTE differences between ceramic (α-alumina) and metallic materials (Al3003). In Fig. 7(b), normal and shear stress components are shown with dotted and solid curves, respectively. It is seen that the stresses at TCB 2 initially increase as temperature increases, then decrease as the temperature continues to increase to 350 °C. It increases again as the system temperature decreases to 20 °C. Note that the sign of stress components simply indicates the direction of stress tensor vectors; therefore, the magnitude of these components is important in predicting mechanical failure. As expected, the circumferential and height shear stresses (σ_{12} and σ_{23} in Fig. 7(b), respectively) are nearly zero at all temperatures, reflecting the cylindrical geometry of the cell. On the other hand, it is clearly predicted that the radial shear (σ_{13}), radial normal (σ_{11}), and circumferential normal (σ_{22}) components are dominant in the contribution to the stress concentrations of TCB 2 surfaces throughout the heating-and-cooling cycles. High stress concentration profiles in the radial and circumferential normal components can be explained by the unconstrained expansion toward those directions. The radial shear stress is particularly important because it is directly related to the interfacial failure of the TCB joints, as previously mentioned. From Fig. 7(b), it is calculated that the local maximum radial shear stress (σ_{13}) occurs after the shutdown process is completed at 20 °C, and it is found that the magnitude of the average maximum radial shear stress is slightly increased as the number of thermal cycle increases, i.e., 77.72 and 79.73 MPa at the completion of first and second shuttingdown processes, respectively. Considering that there is only a small percentage increase in the local maximum values of the average radial stress from the 1st to the 2nd shuttingdown processes, it seems that mitigating the radial stress concentrations upon the first cooling is preferentially important for the interfacial
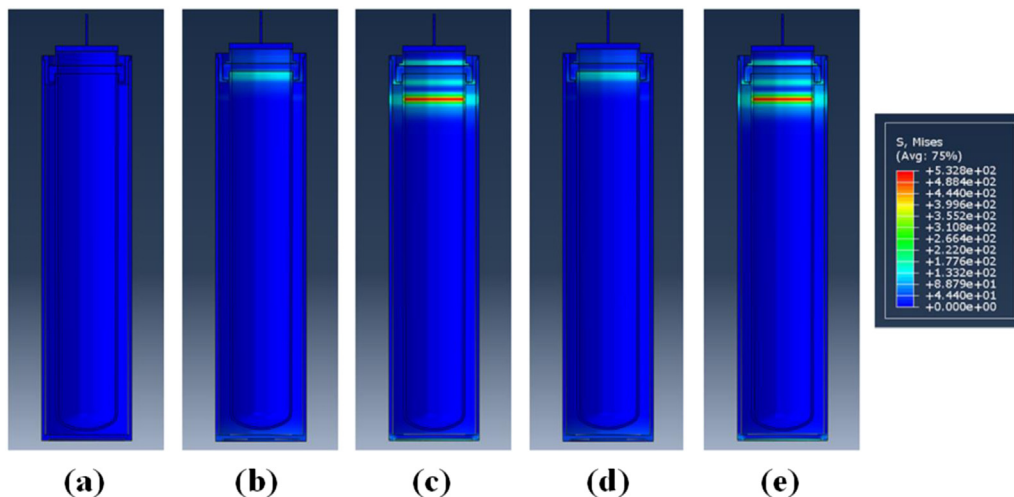

Fig. 6. Example of FEA simulation to show the contour map of von-Mises stress distributions at the temperatures of (a) 20 °C (initial), (b) 350 °C (after the 1st booting), (c) 20 °C (after the 1st shutdown), (d) 350 °C (after the 2nd booting), and (e) 20 °C (after the 2nd shutdown).
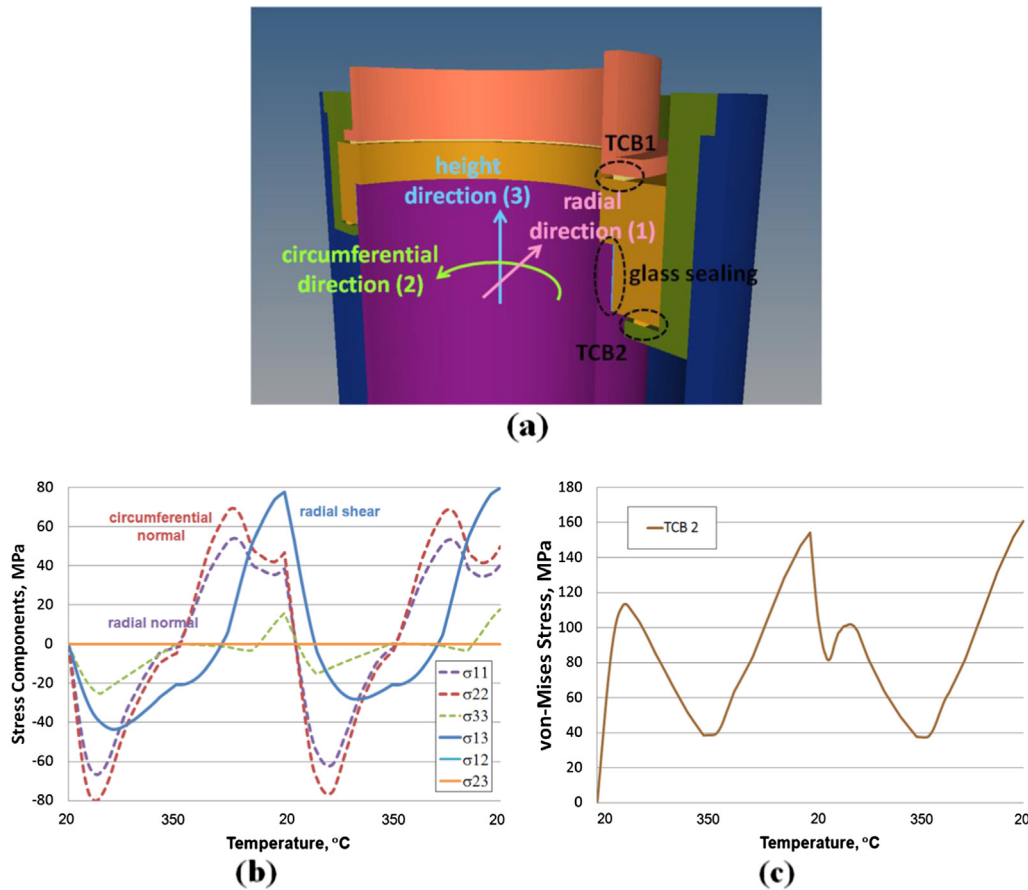
Fig. 7. Stress distributions in TCB 2 of NaS system with Al alloy (Al3003) case materials, (a) schematics to show the stress and strain tensor notations, (b) distributions of averaged six stress components on the top surface of TCB 2, and (c) distribution of averaged von-Mises stress on the top surface of TCB 2.

failure in the TCB areas of the current prototype design. In Fig. 7(c), the von-Mises stress distribution on the top surface of TCB 2 with the simulation time is given. The von-Mises stresses were maximized after the completion of each shuttingdown process, and the magnitude of maximum stress slightly increases as the cycle number increases (from 154.27 to 160.70 MPa for the 1st and 2nd shutdown processes, respectively).

3.2. Interfacial failure between the insert metal and insulating ring at TCB joints

Because the magnitude of radial shear stress concentrations can directly influence the decohesion of the interface between the insert metal and insulating ring, the variations of these radial shear stress distributions were more carefully studied with two different sizes of TCB insert metals. Fig. 8(a) shows the images illustrating two different sizes of TCB 1 metals with widths of 1.5 and 3 mm (1.5 and 3.0 TCB, respectively). With these 1.5 and 3.0 TCB designs, two NaS cells were tested containing one of the two TCB types (1.5 TCB or 3.0 TCB) for each cell. The FEA computation results are given through Fig. 8(b)–(d). The total volumes of two TCB types are identical because the height (0.5 mm) of the narrower 1.5 TCB is twice as large as the height (0.25 mm) of the wider 3.0 TCB. Here, it needs to be pointed out that the results presented in Figs. 6 and 7 are based on the narrower 1.5 TCB design. In Fig. 8(b), the average radial shear stress distributions (σ_{13}) along the bottom surface of TCB 1 and the top surface of TCB 2 are plotted with thermal cycles for the two systems installed with 1.5 and 3.0 TCBs. Again, the average radial shear stress profiles along the surfaces in

contact with insulating ring (the bottom surface of TCB 1 and the top surface of TCB 2) were estimated as these surfaces will suffer from the most severe deformation involving higher possibilities of interfacial decohesion. In the curves of Fig. 8(b), the blue and red color lines (in web version) represent the radial shear stresses from the cells with 1.5 and 3.0 TCBs, and the dotted and solid lines represent the radial shear stresses in TCB 1 and TCB 2, respectively. For these plots, the arithmetically averaged values were obtained from all of the data points on the surfaces of the FEA elements. First, when the average radial shear stresses in TCB 1 and TCB 2 are compared for a given insert metal width, the stresses in TCB 2 (solid lines) are consistently higher than those in TCB 1 (dotted lines). This is because the diameter of TCB 2 is larger than that of TCB 1 from the center axis of the cell along so as to show more deformation. Next, when the average radial stresses in the 1.5 and 3.0 TCBs are compared, the stress concentrations in the 1.5 TCB (blue lines) are much pronounced than those in the 3.0 TCB (red lines). This elucidates that the radial shear stresses resulting from the CTE differences can be more effectively absorbed as the contact area between the TCB and insulator ring becomes larger. Since the curves in Fig. 8(b) show variations of the arithmetically averaged values of the radial stresses, it is necessary to explore the local distributions of σ_{13} upon heating and cooling of the cell. Note that the local stresses are referred to as the stress data calculated in the individual FEA elements. Examination of such local stress distributions will in principle reveal detailed information that could be related to more quantitative fracture behaviors of NaS components. Fig. 8(c) and (d) shows the contour maps that show the variation of the radial shear stresses on the top surfaces of 1.5 TCB 2 and 3.0 TCB
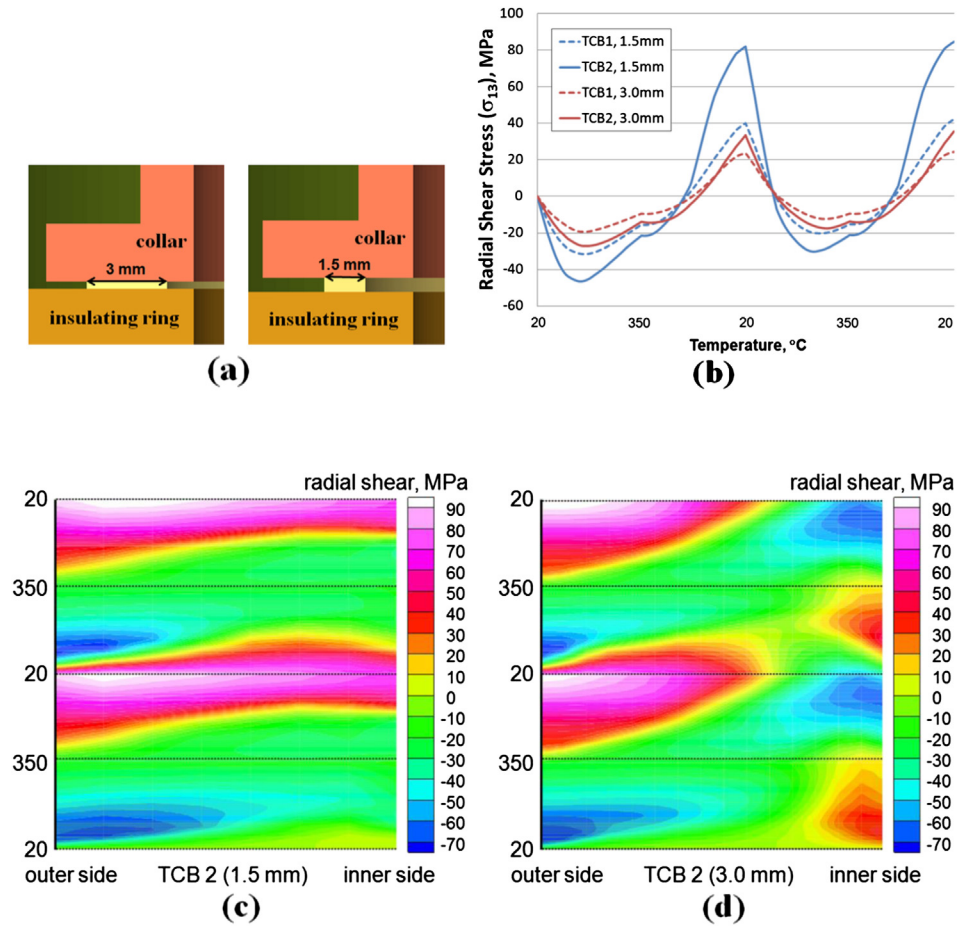
Fig. 8. Radial shear stress (σ_{13}) distributions in the systems with Al3003 case materials. (a) Schematics to show two different sizes of TCB 1 insert metal, (b) average radial shear stress (σ_{13}) distributions along the bottom surface of TCB 1 and the top surface of TCB 2 insert metals with two different sizes shown in (a), and local radial shear stress (σ_{13}) distributions along the top surface of TCB 2 insert metals with widths of (c) 1.5 and (d) 3.0 mm.

2, respectively. The changes of the local positions of 3.0 TCB 2 and the system temperatures are represented along the respective x- and y-axes. In other words, the local σ_{13} distributions with the system temperature changes (equivalently, simulation time) are shown along the vertical y-axis, including localized stress concentration information along the horizontal x-axis. Along the positive direction of x-axis in the contour maps, local σ_{13} variations are illustrated from the outer side to the inner side of a 3.0 TCB 2 top surface. In Fig. 8(c) and (d), the same legend scale was used for simple comparison. Once again, the contact surfaces of TCB 2 were selected here because the radial shear stresses in the TCB 2 surfaces are much more pronounced than those in the TCB 1 surface. Note that although we do not show the analysis results for the TCB 1 surfaces in this manuscript, the general trends of stress distributions predicted in TCB 1 were very similar. From Fig. 8(c) and (d), it is found that, as the cell temperature increases from 20 °C, the outer side of the TCB 2 surface experiences a compressive shear stress (colored as a blue contrast) towards the cylinder symmetry axis of the battery because the ceramic insulator ring possesses a much lower CTE value than the metallic TCB metals. As the system temperature continues to increase to 350 °C and then decrease to 20 °C, the outer side of the TCB metal surface now experiences a tensile shear stress (colored as a red contrast). In particular, the radial shear stresses at the 1.5 TCB joint are mostly greater than ∼70 MPa at the first shutdown (20 °C) throughout the surface, which can lead to a high possibility of interfacial failure between the TCB and the insulating ring. During the 2nd cycle of booting-and-shutdown

process, the trend is repeated and the magnitude becomes larger. Therefore, it is considered that employing wider and thinner TCB metals are one of the most effective methods to curtail the radial shear stress accumulations that can potentially give rise to the bonding decohesion between the ceramic ring and the TCB metals, although other design factors must be also carefully taken into consideration to prevent the interfacial failure during the booting-and-shutdown processes. Based on the results, it is suggested that, for the standard tubular cells, the interfacial shear bonding strength for the TCB joints needs be sufficiently larger than ∼90 MPa to avoid possible interfacial decohesion. However, note that the critical bonding strength to avoid the decohesion could be diminished depending on the bonding geometry. For example, an L-shaped bonding geometry could greatly decrease the required bonding strength at the joints.

In Fig. 9, the distributions of principal plastic strains for the four cases addressed in the previous results in Fig. 8, are presented. The same color and line style scheme was used for Fig. 9 as that of Fig. 8; the average strain profiles on the bottom and top surfaces of TCB 1 and TCB 2 are shown in dotted and solid lines, and the distributions in the narrower 1.5 and wider 3.0 TCBs are shown in blue and red colors, respectively. It is seen in Fig. 9(a) that the general trends of principal plastic strain profiles during the booting-and-shuttingdown cycles for these four different cases are very close to one another; the average principal plastic strain starts increasing near ∼80 °C during the booting process, then it exhibits the local maximum value at the operation temperature (350 °C), and it
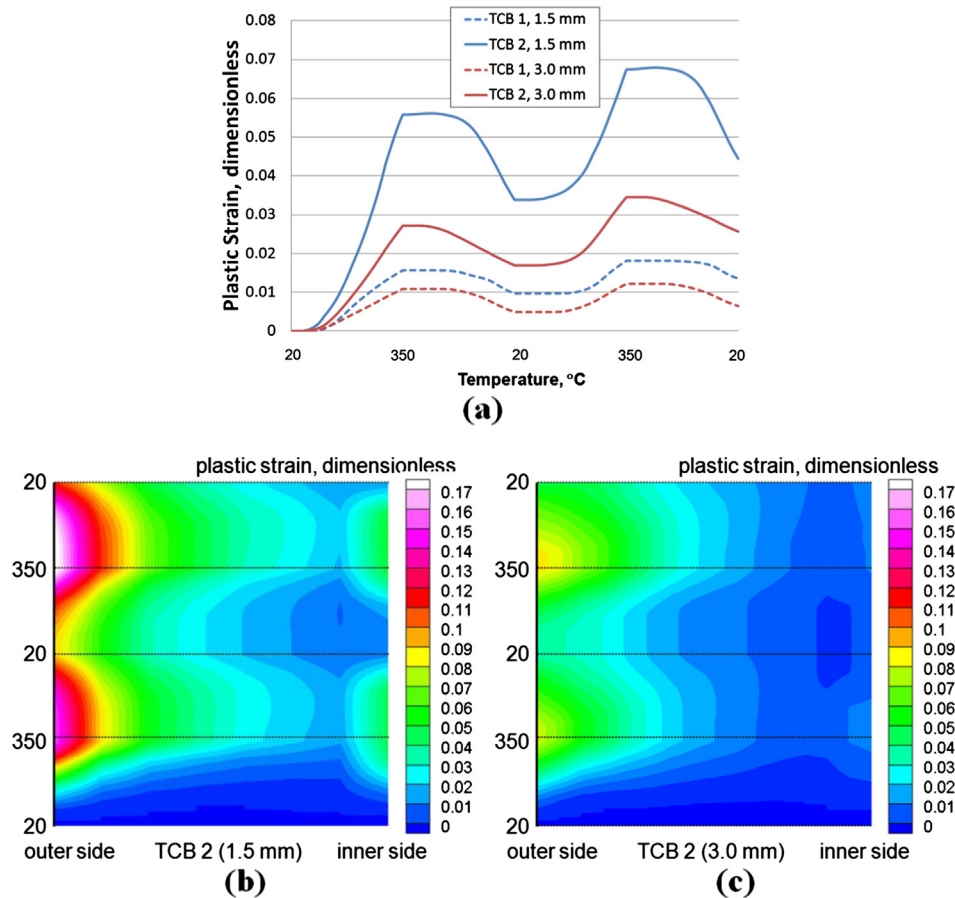
Fig. 9. Principal plastic strain distributions in the systems with Al3003 case materials. (a) Average principal plastic strain distributions along the bottom surface of TCB 1 and the top surface of TCB 2 insert metals with two different sizes, and local principal plastic strain distributions along the top surface of TCB 2 insert metals with widths of (b) 1.5 and (c) 3.0 mm.

decreases as the cell is cooled down to 20 °C. This trend repeats again as the number of booting-and-shuttingdown cycle increases. Also, it can be predicted that the average principal plastic strain will continuously accumulate as the maximum values increase with the number of cycles. The successive accumulation of plastic strains with the number of shutdown cycles is much greater than the successive accumulation of shear stress. This is because the true stress of TCB insert metals (Al3003) does not increase with the true strain at high temperatures as shown in Fig. 4(c). Therefore, although the TCB experiences high plastic deformation in the high temperature range, it does not influence the stress concentrations. Rather, when the system is cooled down, the shear stress is accumulated near the maintenance temperature as found in Fig. 8(b)–(d). Also, it is seen that a much higher plastic strain is accumulated in metallic joints with a larger radius (TCB 2, solid lines) than the ones with a smaller radius (TCB 1, dotted lines), and more plastic deformation is predicted in 1.5 TCB (blue lines) than 3.0 TCB (red lines). For each heating-and-cooling cycle, positions for the maximum shear stress and the maximum principal plastic strain on the TCB surface are different; maximum shear stress is observed after shutdown (20 °C) and maximum plastic strain is seen at the operation temperature (350 °C). The trend is more evident when the information on the local principal plastic strain distributions is provided. In an analog to the two-dimensional analysis presented in Fig. 8(c) and (d), and Fig. 9(b) and (c) show the temporal and spatial plastic strain distributions along the *y*- and *x*-axis, respectively, on the top surfaces of TCB 2 with 1.5 and 3.0 mm widths. Plastic strain distributions in TCB 2 are only included with the same reason explained in the previous

figure; plastic deformations in TCB 2 are much more severe than those in TCB 1. From Fig. 9(b) and (c), it is observed that, in general, the plastic strains in 1.5 TCB 2 (maximum value of 0.178, Fig. 9(b)) are much higher than those in 3.0 TCB 2 (maximum value of 0.088, Fig. 9(c)). As demonstrated in the average plastic strain distribution in Fig. 9(a), the maximum and minimum plastic strains occur at 350 and 20 °C in the local distributions, and the outer side of TCB 2 is subject to a much more pronounced plastic strain. Note that, for the cell design used in this work, the FEA computation predicts that the localized strain concentration can be 2.5–3 times higher than the plastic strain averaged throughout the TCB surface. Based on the results presented in Figs. 8 and 9, it is found that, as the contact area of TCB insert metals is increased, the radial shear stresses and principal plastic strains applied on the surfaces of TCB insert metal can be significantly reduced, which will, in turn, strongly lower the possibility of interfacial decohesion between the insert metal and ceramic insulating ring at the TCB joints.

3.3. Bulk failure of the insulating ring

Another possible failure mechanism at the TCB joints is bulk fracture through the interior region of the insulating ring in the vicinity of the insert metals. It is, therefore, necessary to examine the stress distributions and profiles in the ceramic insulating ring upon heating and cooling of a cell. The two rectangular boxes shown in Fig. 10(a) denote the bottom FEA elements of α-alumina insulating rings that are directly in contact with 1.5 and 3.0 TCBs. The dotted lines indicate the interface between the metallic joints
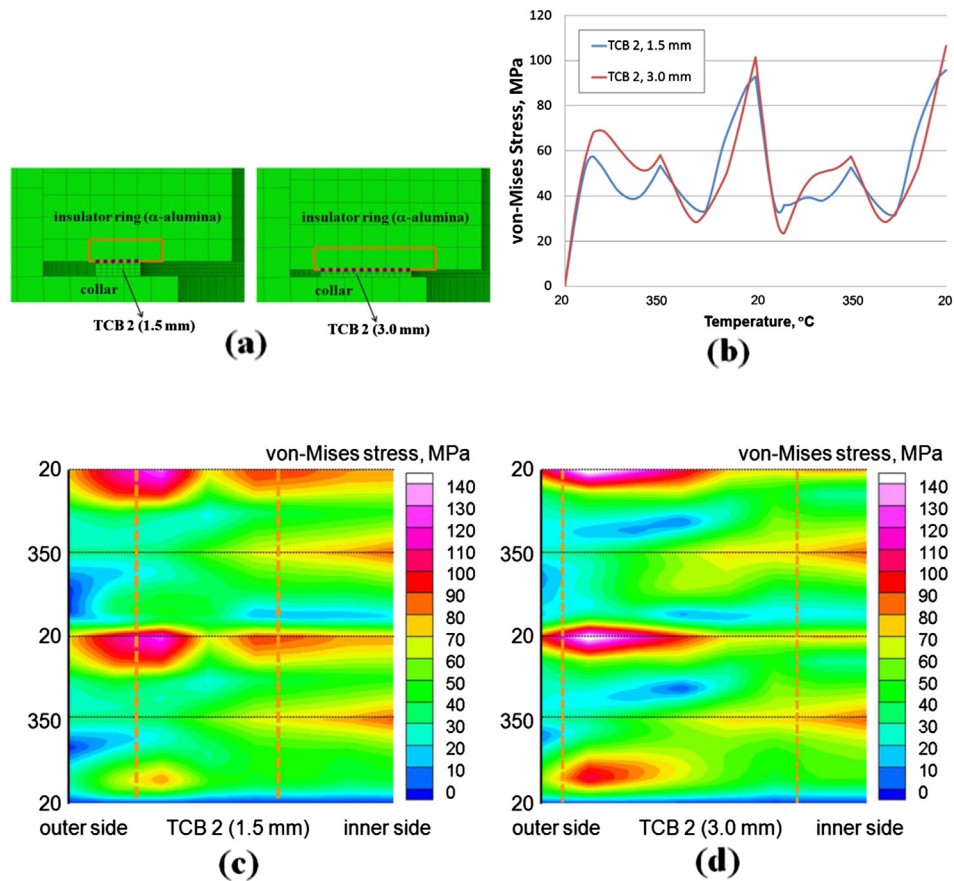
Fig. 10. von-Mises stress distributions in the insulator ring of the systems with Al3003 case materials. (a) Schematics to show two different sizes of TCB 2 insert metals, (b) average von-Mises stress distributions near the bottom surfaces of insulator ring in contact with TCB 2 insert metals of 1.5 mm (blue line) and 3.0 mm (red line) widths, and local von-Mises stress distributions near the bottom surface of insulator ring in contact with TCB 2 insert metals of (c) 1.5 and (d) 3.0 mm widths. (For interpretation of the references to color in this figure legend, the reader is referred to the web version of this article.)

and the ceramic insulator. Because these localized areas will experience the most severe stress aggregations, the average von-Mises stress profiles in these elements (i.e., three and five FEA mesh elements enclosed in the orange boxes (in web version) in Fig. 10(a) for the systems with 1.5 and 3.0 TCB 2, respectively) with the temperature change are given in Fig. 10(b). In this case, plots for the average von-Mises stress distributions are shown because the bulk fracture through the interior side of the insulator ring can be estimated from the Griffith fracture criterion [11] assuming no plastic deformation for the ceramic insulator ring. Here, the average stress variations near the bottom surface are analyzed because the stresses were found to be much higher near the bottom side of the ring that is in touch with TCB 2 than those in the top side adjacent to TCB 1. Keep in mind that the von-Mises, radial shear stress, and plastic strain data included in the previous section (Figs. 7—9) are extracted from the surface of the FEA mesh element, while the calculation of the von-Mises stress shown in Fig. 10(b) is based on the center point of the mesh elements so as to represent the pseudo-bulk properties adjacent to TCBs. In Fig. 10(b), although the difference is not notable, it is observed that the average von-Mises stress is higher near the bottom region of the insulator ring in the system with 3.0 TCB 2 (red line) than the 1.5 TCB 2 (blue line) in the majority of the temperature ranges. With 3.0 TCB 2, the maximum average von-Mises stresses are predicted as approximately 101 and 106 MPa for the 1st and 2nd booting procedures, respectively. In Fig. 10(c) and (d), local variations of these von-Mises stresses in the bottom FEA element of insulator rings in contact with 1.5 and 3.0

TCBs are plotted along the geometrical positions and the temperatures in the x- and y-axis, respectively. In these contour maps, all of the stress calculations from the entire bottom elements are displayed along the x-axis, and the dotted lines in Fig. 10(c) and (d) denote the boundaries of the FEA elements of the insulator rings that are directly in contact with TCB 2 and those that are not in contact with TCB 2 metals. Therefore, the von-Mises stresses shown in Fig. 10(b) are the arithmetically averaged values of the data contained inside the dotted lines. From Fig. 10(c) and (d), it is clearly predicted that the maximum stress concentration occurs near the outer side of the TCB joints, and that the local stress is also higher for most of the parts in the system with 3.0 TCB 2. The maximum stress aggregation point is given as slightly on the inner side of the TCB 2 boundary line for both sets because the maps are constructed relying on the data from the center points of FEA elements. With 3.0 TCB 2, the local maximum von-Mises stress is estimated at 151 and 154 MPa for 1st and 2nd booting procedures, respectively. These results are important because, considering that the fracture strength of α-alumina used in this study ranges between 300 and 450 MPa, the bulk failure through the interior region of the α-alumina insulating ring is not expected to occur for the present cell design. However, it should be noted that since the fracture strength of the ceramic material is strongly influenced by the microstructural features such as grain size, fracture energy, and internal crack size/distribution, careful examination must be carried out to more accurately quantify the fracture strength of these materials.

3.4. Effects of container materials

For another type of NaS cells, we hypothetically altered the container material from an Al alloy (Al3003) to a stainless steel (STS430). As mentioned in "Materials properties" section, either an Al alloy or a stainless steel can be selected for a container material, and STS430 is one of the possible candidate alloys for the cell container of a NaS cell. In applying STS430 as a container material, it should be noted that the CTE and modulus of STS430 are much closer to those of α- or β-alumina, and thus, a much smaller amount of deformation and resultant stress is expected to aggregate at the TCB joints. The material properties can be found in Fig. 4(a) and (b). In addition, as for the true stress–strain relationships in Fig. 4(c) and (d), while Al3003 exhibits wider stress profile variations depending on the measured temperature, STS430 curves have relatively narrower temperature variations except at room temperature (20 °C). As previously pointed out in describing the results of Fig. 9, the true stresses of Al3003 do not increase with strains at higher temperatures, but the stresses of STS430 continuously increase with increasing strain over all temperatures of 20–350 °C. Such differences in thermo-mechanical and physical properties of Al3003 and STS430 can lead to a substantial difference in the thermal stress accumulations at the TCB area of a NaS cell. Fig. 11 compares the radial shear stress distributions on the TCB 2 top surfaces with the two distinct container materials as well as two types of TCBs (1.5 TCB and 3.0 TCB). In Fig. 11(a), the curves with

long dots represent the average radial shear stress profiles of 1.5 and 3.0 TCB 2 (green and orange lines (in web version), respectively) in the cell with STS430, and they were compared with those from the cell with Al3003 container, as indicated by the solid curves corresponding to 1.5 and 3.0 TCB 2 (blue and red lines, respectively). Comparing the solid and dotted curves for each TCB type, it can be seen that the magnitude of shear stress is generally deceased by adopting STS430 container materials. At 20 °C, after the 2nd shutdown cycle, the maximum average radial shear stresses are decreased from 85 (blue) to 52 (green) MPa and from 35 (red) to 23 (orange) MPa in the surfaces of 1.5 and 3.0 TCB 2, respectively. One more point to be addressed is that when STS430 is used combined with the 3.0 TCB geometry, the peak shear stress position occurs at the operation temperature (350 °C), not at the maintenance temperature (20 °C), in the 1st booting-and-shutdown cycle. Also, note that the maximum average stress on the TCB surface is greater in the system with STS430 than Al3003, although the difference is not large. It is important because the system temperature will be maintained at the operation temperature for several years after the 1st booting; therefore, using STS430 can involve more adverse effect that can give rise to the interfacial decohesion during the normal operation, which might lead to a catastrophic failure in the grid system level.

In Fig. 11(b) and (c), we display the results of contour maps containing the local variations of the radial shear stresses on the top surfaces of 1.5 and 3.0 TCB 2 in the position-temperature space.
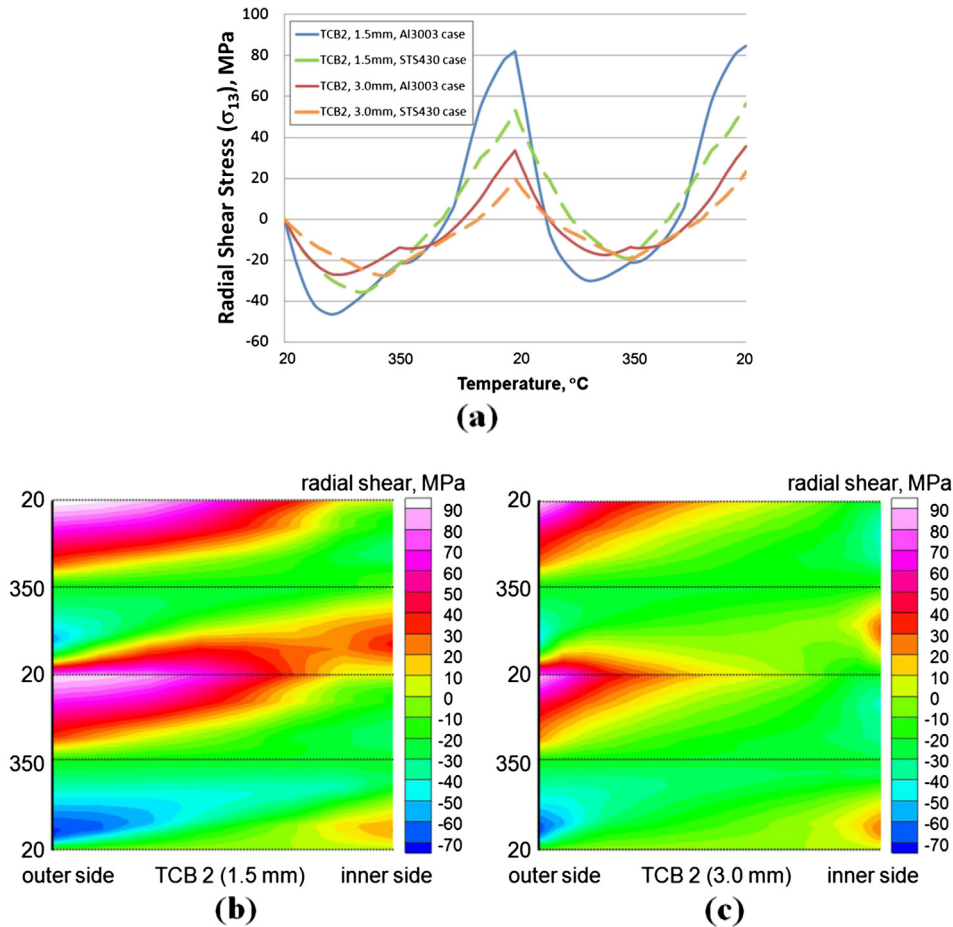

Fig. 11. Radial shear stress (σ_{13}) distributions in the systems with STS430 container materials. (a) average radial shear stress (σ_{13}) distributions along the top surfaces of TCB 2 insert metals with two different sizes and two different battery case materials, and local radial shear stress (σ_{13}) distributions on the top surface of TCB 2 insert metals with widths of (b) 1.5 and (c) 3.0 mm.

When these localized radial shear stresses in Fig. 11(b) and (c) are compared with their corresponding counterparts from Al3003 container materials (i.e., Fig. 8(c) and (d) for 1.5 and 3.0 TCB 2, respectively), while the peak position of shear stress remains the same at the outer side upon shutdown to 20 °C, it is manifestly seen that the overall areas of high radial shear stress (over ~50 MPa, pink contrast region) have been much reduced. This indicates that the radial shear stresses that can lead to the interfacial decohesion between the insulating rings and the TCB metal joints can be greatly lowered by using a STS430 battery container. Considering that the typical bond strengths between the insulating rings and the Al alloy insert metals sit in the range of 15−35 MPa in normal stress and 80−200 MPa in shear stress, it is predicted that the cell using a 1.5 TCB 2 and Al3003 container will have a high probability of interfacial shear decohesion during cooling. Alternately, when the 3.0 TCB 2 and STS430 battery container materials are used, the probability of interfacial fracture in this vulnerable region would be considerably lowered, but there still is a localized region near the outer side of 3.0 TCB 2 that suffers from high shear stress accumulation over ~50 MPa. In any case, the local maximum shear stress is calculated as ~90−95 MPa at the end of the 2nd shutdown stage. Therefore, it is suggested that the shear strength between the insulator ring and the TCB 2 interfaces must be greater than 100 MPa to reconcile the multiple cycles of booting-and-shutdown processes for the system considered in the present work. Otherwise, a careful design regarding material types and components structural geometries must be accompanied to successfully relieve the stress concentration and to secure the safety from the thermo-mechanical failure. For this purpose, stress damping structures are often included using a groove or spring type geometry in the cell container structure. Currently, an advanced prediction model development incorporating such stress damping geometries is in progress, which will be presented in a later paper. As shown in Fig. 11, it is thought that the absorption of thermal stress has to be carefully conceived when a cell structure is designed using Al alloys. STS430 has much lower CTEs compared with Al3003 to reduce the CTE difference at the TCB joints, although it is more expensive and has inferior machinability to Al alloys. Although we do not focus on the thermo-mechanical behaviors of GS joints bridging the insulating ring and β/β″-alumina solid electrolyte in the present work, the GS also have to be very carefully selected to minimize the stress concentration at the joint. We will discuss the stress field in the glass sealing joint region in a later paper as well.

Finally, we show the contour maps to include the local von-Mises stress distributions using the position-temperature space in

the bottom area of the insulating ring in contact with (a) 1.5 TCB 2 and (b) 3.0 TCB 2, when STS430 was used as the battery container materials. The maps in Fig. 10(c) and (d) are the direct corresponding counterparts with those in Fig. 12(a) and (b), respectively. For easy comparison, a same legend scale was used in Fig. 10(c) and (d) and Fig. 12(a) and (b). When the local von-Mises stress distributions are compared with each other for the systems containing Al3003 and STS430 battery cases/containers, it is seen that the von-Mises stress concentrations are much alleviated by incorporating STS430 due to the smaller differences in the displacements of TCB metals and insulator rings. After the 2nd shutdown at 20 °C, the local maximum von-Mises stresses in the insulator ring in touch with 3.0 TCB 2 from the systems using Al3003 and STS430 container materials are predicted as 154 and 107 MPa, respectively. It needs to be pointed out that these von-Mises stress ranges are much lower than the bulk fracture strength of α-alumina materials, assuming that no major cracks exist in the insulating ring that can significantly lower the fracture strength. Hence, the FEA computation demonstrates that the primary failure mechanism in the tubular NaS system design considered in the current work would be the interfacial fracture that can take place between the insulator ring and the TCB 2 insert metals, and the necessary treatments, including new system designs or better material selection, must be involved to avoid the fractures of constituent components/parts in the TCB area. More realistic FEA models are currently under development with sophisticated hypotheses and assumptions, such as considerations of realistic cathode materials (sulfur and Na_2S_x), local distributions during heating and cooling, and of application of realistic local temperature profiles rather than complete isothermal temperature changes.

4. Summary

Mechanical failures and disintegrations at the TCB joints are one of the major issues in developing advanced large sized NaS cells with enhanced safety for grid-scale applications. Quantitative understanding of the relationships among the structural constituents, geometrical designs, and the resultant stress concentrations in these metal-ceramic joints is essential. In this paper, we introduce a computational FEA model to predict the stress concentrations within the tubular NaS cells. The computational tool presented in this work is considered one of the first approaches to address the mechanical failure issues in the header area of medium-large sized tubular NaS batteries. Throughout the "Result and discussion" section in this document, we have shown that how the developed
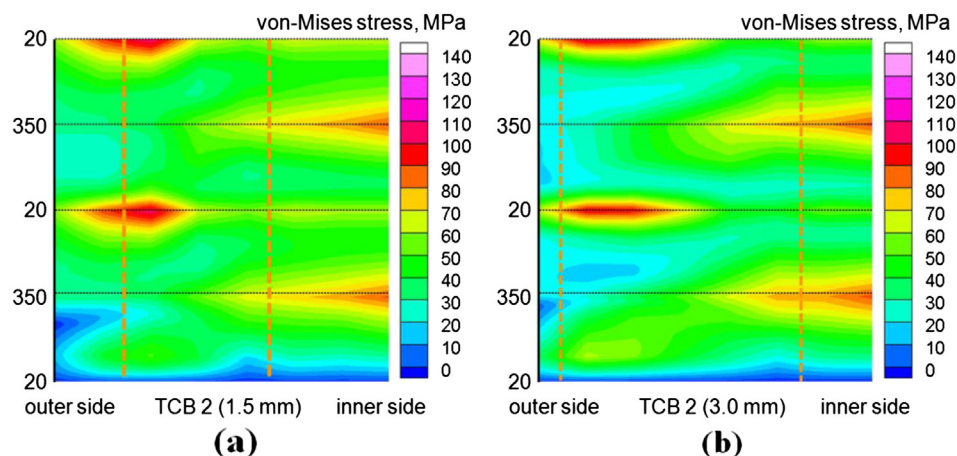

Fig. 12. von-Mises stress distributions in the systems with STS430 container materials. Local von-Mises stress distributions near the bottom surfaces of insulator ring in contact with TCB 2 insert metals of (c) 1.5 and (d) 3.0 mm widths.

computational tool can be applied to the analysis of thermo-mechanical stability and provide a guideline to improve the robustness of NaS cells. Using the computational model developed here, the results based on our prototype system design are summarized as follows.

- During the booting-and-shutdown thermal cycles, the radial shear stress concentration at the TCB joints is predicted as high as 80–95 MPa for a cell with an Al alloy container, which can cause interfacial failure along heterogeneous interfaces.
- The von-Mises stress concentration of the insulating ring near the TCB joints is calculated as high as 100–150 MPa for a NaS cell with an Al alloy container. Therefore, it is thought that the bulk fracture would not be a major route to a cell failure for the present design.
- By increasing the interfacial contact area at the TCB joints, the radial shear and von-Mises stress concentrations can be considerably reduced. For example, the maximum values of the average radial shear stress on the surface of TCB 2 joints in touch with the insulator ring have been decreased from ~ 80 to ~ 30 MPa by increasing the width of TCB from 1.5 to 3.0 mm.
- By changing the container materials from Al alloys (Al3003) to stainless steels (STS430), both the radial shear and von-Mises stress concentrations are greatly reduced; however, there still are some localized areas in the outer side of the TCB surface that will experience relatively strong radial shear stress concentrations over ~ 50 MPa.

It is concluded that the thermo-mechanical shear stresses must be absorbed by incorporating elaborately selected materials and/or by altering the cell geometries, and sufficient bonding strength between the insulating ring and TCB insert metal is required to endure the thermal stress arisen by thermal cycles. Although it is expected that there are some variations in the geometrical design for a large size tabular NaS cell, the results obtained throughout the present work can provide useful insights toward much safer NaS cells. Further, it is envisaged that the computational model developed though the current effort can be readily applied to other NaS system designs interfaced with various material types, including metals and ceramics, and it could provide guidance for the material selection and system design to minimize the stress concentrations in the TCB insert metal sealing joints of medium-to-large size NaS batteries.

Acknowledgments

References

[1] N. Weber, J.T. Kummer, Sodium–sulfur secondary batteries, in: Proceedings of the 21st Annual Power Sources Conference, Monmouth, NJ, 1967.
[2] X. Lu, G. Xia, J.P. Lemmon, Z. Yang, J. Power Sources 195 (2010) 2431–2442.
[3] B.L. Ellis, L.F. Nazar, Curr. Opin. Solid State Mater. Sci. 16 (2012) 168–177.
[4] B. Dunn, H. Kamath, J.-M. Tarascorn, Science 334 (2011) 928–935.
[5] T. Oshima, M. Kajita, Int. J. Appl. Ceram. Technol. 1 (2004) 269–277.
[6] J. Sangster, A.D. Pelton, J. Phase Equil. 18 (1997) 89–96.
[7] T.B. Kim, J.W. Choi, H.S. Ryu, G.B. Cho, K.W. Kim, J.H. Ahn, K.K. Cho, H.J. Ahn, J. Power Sources 174 (2007) 1275–1278.
[8] X. Lu, B.W. K, W. Xu, G. Li, J.Y. Kim, J.P. Lemmon, V.L. Sprenkle, Z. Yang, Energy Environ. Sci. 6 (2013) 299–306.
[9] J. Wang, J. Yang, Y. Nuli, R. Holze, Electrochem. Commun. 9 (2007) 31–34.
[10] Atlas of Stress–Strain Curves, second ed., ASM International, 2002.
[11] A.A. Griffith, Philos. Trans. R. Soc. Lond. A221 (1921) 163–198.